ELSEVIER

Nuclear Instruments and Methods in Physics Research A 457 (2001) 52–63

NUCLEAR INSTRUMENTS & METHODS IN PHYSICS RESEARCH Section A

www.elsevier.nl/locate/nima

Chromatic aberration and forward scattering of light in silica aerogel

R. De Leo[a,*], V. Capozzi[b], C. Casalino[a], E. Cisbani[c], C. Coluzza[d], S. Frullani[c], F. Garibaldi[c], M. Iodice[c], L. Lagamba[a], E. Nappi[a], G. Perna[b], G.M. Urciuoli[c]

[a]*INFN, Sezione di Bari, e Dipartimento Interateneo di Fisica, Universita degli Studi di Bari, via Amendola 173, I-70126 Bari, Italy*
[b]*INFM, Unità di Bari, e Dipartimento Interateneo di Fisica, Universita degli Studi di Bari, via Amendola 173, I-70126 Bari, Italy*
[c]*INFN, Gruppo Sanità, e Laboratorio di Fisica dell'Istituto Superiore di Sanità, viale Regina Elena 299, I-00161 Roma, Italy*
[d]*INFN, Sezione di Roma 1, e Dipartimento di Fisica dell'Università 'La Sapienza', I-00100 Roma, Italy*

Received 17 December 1999; accepted 11 March 2000

Abstract

The scattering of light at small angles (not Rayleigh) and the dependence of the refractive index of silica aerogel produced by the Matsushita Electric Works (Japan) on wavelength were investigated in the range of interest for Ring Imaging Cherenkov detectors (RICH). In the λ-interval 350–650 nm, the aerogel refractive index decreases by 0.15%, the average forward scattering angle of light in traversing aerogel varies from 1.2 to 2.2 mrad, and the fraction of forward scattered light per cm of aerogel varies from 20% to 8%.

PACS: 29.40.Gx; 29.40.Ka

Keywords: Aerogel; RICH; Optical properties

1. Introduction

The use of silica aerogel in RICH detectors is recent and follows from the development of high-quality samples produced with a new technique [1,2] by Matsushita Electric Works (Japan).

In 1995, Seguinot and Ypsilantis proposed [3] an appealing application of aerogel in the LHCb experiment [4]. The outstanding potential of their design inspired the upgrade [5–8] of the HERMES experiment [9] at DESY.

So far, the literature has mostly been devoted to the calculation of the number of photoelectrons (pe) achievable in a ring [10–13] Only a rough estimation has been given [12,13] of the precision that could be obtained with the reconstruction of the Cherenkov angle, which affects the resolution power of the detector when identifying different particles.

This paper deals with a more precise estimation of two contributions to the Cherenkov angle resolution, namely the chromatic aberration and the angle dispersion due to 'forward scattering' (FS) of light in aerogel. Whilst Rayleigh scattering, the main source of background in aerogel Cherenkov imaging, is responsible for the bluish haze that

* Corresponding author. Tel.: +39-80-54-43-242; fax: +39-80-55-34938.

E-mail address: deleo@ba.infn.it (R. De Leo).

0168-9002/01/$ - see front matter
PII: S0168-9002(00)00668-9

surrounds aerogel, FS is responsible for the sometimes fuzzy, sometimes deformed images of objects viewed through aerogel.

This paper is organized as follows. Section 2 describes the measurement of the refractive index of aerogel (of nominal value 1.03 at 633 nm) at six wavelengths in the range 350–650 nm, and the influence of the chromatic aberration on the Cherenkov angle measurement. Section 3 describes the measurement of the average FS deflection angle of light in aerogel, and the fraction of deflected light per centimetre of crossed aerogel. These measurements are employed to evaluate the FS contribution of the resolution. The fraction of light deflected at forward angles is evaluated in a different way in Section 4 by using a spectrophotometer supplied with an integrating sphere. From these measurements, the aerogel FS length (Λ_{FS}) is deduced in the interval from 200 to 900 nm and compared with the aerogel absorption and Rayleigh scattering lengths ($\Lambda_{A,S}$) determined in a recent paper [11]. Contributions to the Cherenkov angle resolution of the HERMES and LHCb RICH detectors are briefly reviewed in Section 5, and the conclusions of the paper are given in Section 6.

2. Dependence of the refractive index of aerogel on wavelengths

The method of 'minimum deflection' was used to measure the refractive index (n) of aerogel

$$n = \frac{\sin(\phi/2 + \alpha/2)}{\sin(\phi/2)} \quad (1)$$

where ϕ is the apex angle of the tile corner used for the measurement, and α is the minimum deflection angle.

The method provides an accurate measurement of n since it involves very low systematic errors. The uncertainty in n is linked to that of the two angles ϕ and α. The latter is determined from two measurements of the distances, $\tan\alpha = d/L$, where d is the 'minimum distance' determined on a screen placed at a distance L from the aerogel. In the approximation $d \ll L$, it follows that

$$\left(\frac{\Delta n}{n}\right)^2 = \frac{1}{4}\frac{[(d/L)^2\{(\Delta L/L)^2 + (\Delta d/d)^2\}]}{\tan^2(\phi/2 + \alpha/2)} + \frac{1}{4}\left[\frac{\sin(\alpha/2)}{\sin(\phi/2)\sin(\phi/2 + \alpha/2)}\right]^2 (\Delta\phi)^2. \quad (2)$$

For distances and apex angles measured with small uncertainties ($\Delta d = \Delta L = 1.5$ mm, and $\Delta\phi = 0.1^\circ$) systematic errors of 0.015% in n can be achieved when $L = 3.5$ m. To obtain these uncertainties in the measurements of d, lasers with a small spot and divergence must be employed, as well as aerogel tiles with well defined and regular corners. A drawback of this method is that a large deformation of the laser spots prevents the measurements of n in the central region of a tile. The refractive index has been measured in a Matsushita tile with dimensions $11 \times 11 \times 1$ cm^3.

To limit the uncertainties in determining the minimum distance at the different wavelengths, the measurements were performed with two overlapping laser beams. An He–Ne laser at 633 nm, with a divergence of 1 mrad, was used as the reference. The measurements at 514, 496, and 458 nm were performed by an Ar-ion laser with a divergence of 1.5 mrad. An He–Cd laser, with a divergence of 1.5 mrad, was used for the measurements at 422 and 325 nm. The measurements were repeated many times at different points of the lateral surfaces (sizes 1×11 cm^2) of the aerogel tile, close to the four corners.

The distributions of the measurements performed are reported in Fig. 1 at the wavelengths indicated. The solid lines in Fig. 1 are Gaussian fits to the distributions. The mean n values extracted from these distributions are reported in Fig. 2. The values at 633 and 514 nm differ by 3×10^{-4}. This difference is in agreement with a previous measurement at the two wavelengths [12,13]. The total variation measured for n in the λ-range explored is only 0.15%, and the measurement at 325 nm contributes to half of this variation.

The n value at 633 nm of the examined tile is 1.0298, while the average value of all the tiles employed in the HERMES RICH, measured at the same wavelength, resulted in 1.0304 ± 0.0004.

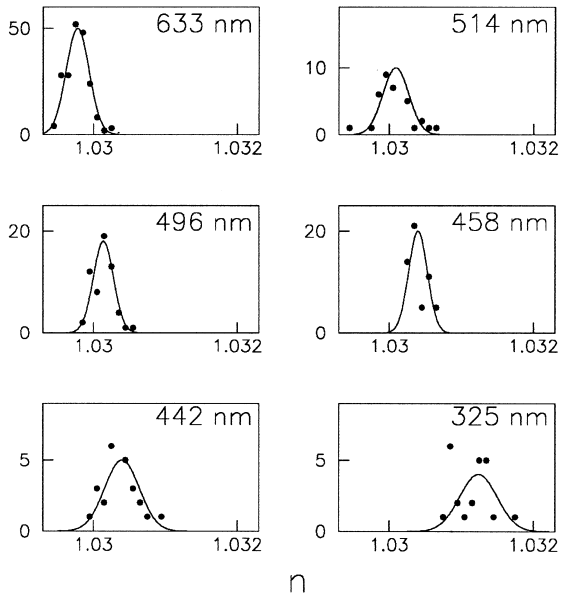

Fig. 1. The distributions of the refractive index (n) measurements of a Matsushita aerogel tile at the wavelengths indicated. The solid lines are Gaussian fits to the distributions. The higher statistics at 633 nm are due to the use of this wavelength as the reference source (see text).

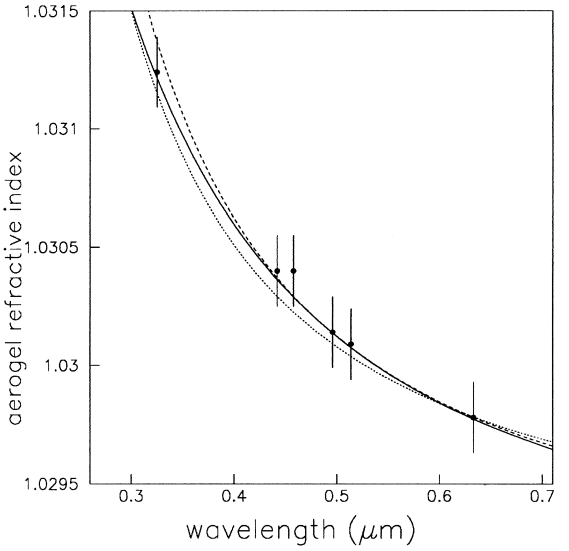

Fig. 2. The refractive index of one Matsushita aerogel tile measured at six wavelengths. The solid, dashed, and dotted lines are fits to the experimental data based on Eqs. 3, 4, and 7, respectively, with calculated values normalized to the experimental value of the refractive index of aerogel at 633 nm.

The standard deviations of the n-mean values in Fig. 1 are small. Therefore, the errors reported on the experimental points in Fig. 2 are the systematic ones. The fit of the data with a phenomenologic function

$$n = C + C'/\lambda^x \tag{3}$$

represented by the solid curve in Fig. 2, gives the following λ-dependence of n: $x = 1.2 \pm 0.2$.

Vorobiov et al. [14] suggested that the λ-dependence of n in aerogel (n_{aerogel}) could be derived by those of air (n_{air}) and quartz (n_{SiO_2}), the main components of aerogel, whose refractive indices are well known [14] in the λ-range investigated here. If n_{aerogel} is experimentally measured at one reference wavelength λ_0, the differences between $n_{\text{aerogel}}(\lambda_0)$, $n_{\text{air}}(\lambda_0)$, and $n_{\text{SiO}_2}(\lambda_0)$ can be employed at other wavelengths to deduce the λ-dependence of n_{aerogel}:

$$n_{\text{aerogel}}(\lambda) = An_{\text{SiO}_2}(\lambda) + (1 - A)n_{\text{air}}(\lambda) \tag{4}$$

where

$$A = \frac{n_{\text{SiO}_2}(\lambda_0) - n_{\text{aerogel}}(\lambda_0)}{n_{\text{SiO}_2}(\lambda_0) - n_{\text{air}}(\lambda_0)}. \tag{5}$$

By assuming for reference (λ_0) the upper limit of the investigated interval (633 nm), the fit displayed in Fig. 2 with a dashed line and an A value of 0.0646 are obtained.

A better estimation of the λ-dependence of n_{aerogel} is based on the Lorentz–Lorenz theory [15]. The refractive constant (R) for a material of density ρ is defined as

$$R = \frac{n^2 - 1}{n^2 + 2}\frac{1}{\rho}. \tag{6}$$

In a compound, the refractive constants of components multiplied for their partial weights (P_i) are additive, i.e. $PR = P_1R_1 + P_2R_2$, where $P = P_1 + P_2$. Then

$$\frac{n^2_{\text{aerogel}} - 1}{n^2_{\text{aerogel}} + 2} = B\frac{n^2_{\text{SiO}_2} - 1}{n^2_{\text{SiO}_2} + 2} + (1 - B)\frac{n^2_{\text{air}} - 1}{n^2_{\text{air}} + 2} \tag{7}$$

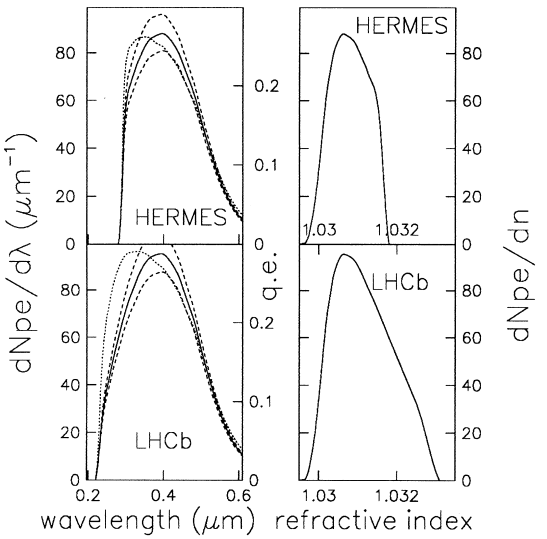

Fig. 3. Left-side panels: Number of detected Cherenkov photons (solid lines), with estimated uncertainties (dashed lines), as a function of the photon wavelength, calculated according to Ref. [11] for a stack (5 cm) of aerogel ($n = 1.0304$). The dotted curves represent the quantum efficiency typical of bialkali photocathodes, corrected, in the top panel (HERMES) for transmittance through 3 mm of a Lucite foil, and in the bottom panel (LHCb) through a Mylar window. Right-side panels: Number of detected Cherenkov photons as a function of the aerogel refractive index.

where B is the fraction of the volume occupied by quartz in aerogel. The λ-dependence of n_{aerogel}, deduced from Eq. (7), is displayed in Fig. 2 with a dotted line.

By comparing the dashed lines, dotted ones, and experimental values in Fig. 2, it can be seen that both the aforementioned hypotheses are able to predict the λ-dependence of n_{aerogel}. Measurements of n_{aerogel} with a lower systematical error and in a more extended λ-interval than explored here could assess which of the two hypotheses is more suitable for aerogel.

By weighting the λ-dependence of n_{aerogel} (solid line) with that of the photoelectrons from the unscattered Cherenkov radiation, the quantity n_{aver} can be estimated

$$n_{\text{aver}} = \frac{\int n(\lambda)(\mathrm{d}N_{\text{pe}}/\mathrm{d}\lambda)\,\mathrm{d}\lambda}{\int(\mathrm{d}N_{\text{pe}}/\mathrm{d}\lambda)\,\mathrm{d}\lambda}. \tag{8}$$

The λ-dependence of photoelectrons for the HERMES and LHCb RICH detectors are reported in the left panels of Fig. 3 with solid lines. The dotted lines are an estimation of the uncertainties. The photoelectrons were evaluated in accordance with Ref. [11], for 5 cm of $n = 1.0304$ aerogel with a 3 mm thick Lucite window for the HERMES RICH, and a Mylar window for the LHCb one. The quantum efficiency (q.e.) of typical bialkali photocathodes, corrected for the transmittance of the relative exit window, is reported in the left panels of Fig. 3 with dot-dashed lines. The different exit window, is responsible for the UV more extended bandwidth of LHCb. This can be seen more clearly in the right panels of Fig. 3 where the n-distributions of photoelectrons are reported.

The values $n_{\text{aver}} = 1.0306$ for HERMES, and 1.0308 for LHCb, were obtained for the examined tile. A difference of $\Delta n = 0.0008$ for HERMES and 0.0010 for LHCb is then deduced for n_{aerogel} from the measurements at the reference wavelength of 633 nm and its value at 400 nm, the centre of the photoelectron distributions in Fig. 3.

The n_{aerogel} values, averaged over all the tiles and at the centre of the photoelectron distributions, are: $n_{\text{aver}} \pm \sigma_n = 1.0312 \pm 0.00046$ for HERMES, and 1.0314 ± 0.00066 for LHCb.

The contribution of the chromatic aberration to the resolution of the RICH is obtained from the relation

$$\left(\frac{\delta\theta}{\theta}\right)_{\text{chromatic}} = \frac{1}{2}\left(\frac{\sigma_n}{n_{\text{aver}} - 1}\right)\frac{1}{\sqrt{N_{\text{pe}}}}. \tag{9}$$

From the integrals of the curves in Fig. 3, the total number of photoelectrons (N_{pe}) are obtained: 18 ± 2 for HERMES, 23 ± 3 for LHCb. These numbers are overestimated since the photon absorption factors behind the aerogel (reflectivity of the mirrors and geometrical acceptance of active elements in the focal plane) are not considered.

For HERMES, $N_{\text{pe}} = 9$ was found experimentally. From the previous n_{aver} and σ_n values, a chromatic aberration of $(\delta\theta/\theta)_{\text{chromatic}} = 0.26\%$ is evaluated for HERMES. In the LHCb project, 15 photoelectrons are expected. This results in a chromatic aberration of 0.27%.

3. Forward scattering of light in silica aerogel

In Ref. [16], it has been shown that in an inhomogeneous medium, like silica aerogel, the intensity of the light scattered at small angles depends on the microscopic density fluctuations which cause local variations of the dielectric properties of the material. In contrast to the nearly isotropic Rayleigh scattering, which depends on the average molecular dimension, the anisotropy in the dielectric constant of the medium causes a light scattering which is strongly forward peaked, and, consequently, contributes to the angular dispersion of the light. It has also been shown in Ref. [16] that the ratio between the two types of scattering is strongly dependent on the pH of the base solution from which the silica aerogel is catalysed. Moreover, the FS comes mostly [16] from the boundaries of the aerogel tile crossed by light (surface effect), in contrast with the Rayleigh scattering which is proportional to the thickness traversed by light in aerogel (volumetric effect).

For practical purposes, FS is more important than Rayleigh scattering. Indeed both the HERMES and LHCb detectors envisage reducing the Rayleigh isotropic background by decreasing the detector bandwidth in the UV region by placing a Lucite or a Mylar window downstream of the aerogel to absorb most of the scattered photons. In contrast, FS affects a large fraction of the Cherenkov photons in the whole wavelength range (as will be shown later) and cannot therefore be minimized.

The FS measurements were performed at the six aforementioned laser wavelengths. A photodiode with an active area of $15 \times 15\ \mathrm{mm}^2$, placed 1 m from the laser source, as shown in Fig. 4, was used as the detector. A diaphragm with a variable aperture, placed in front of the photodiode and centred on each beam, was used to measure the amount of light transmitted as a function of the diaphragm aperture.

Each measurement was taken with the photodiode centred on the maximum intensity of the transmitted beam. In this way deflections of the beam caused by non-parallelism of the tile surfaces are avoided.

The red ($\lambda = 633$ nm) laser beam intensity [$T_0(\theta)$, displayed by squares in Fig. 5], and the transmittances measured with one [$T_1(\theta)$, circles], or two [$T_2(\theta)$, triangles] aerogel tiles interposed in the beam are reported in the top panel of Fig. 5 as a function of the diaphragm opening angles.

The measured transmittances change rapidly as one moves the aerogel point hit by the beam.

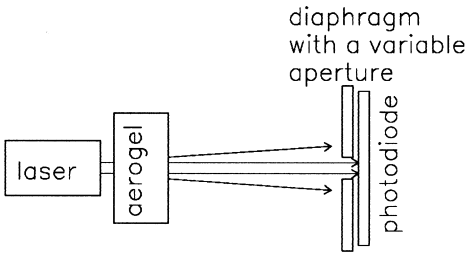

Fig. 4. Schematic drawing of the apparatus used for measuring the forward scattering.

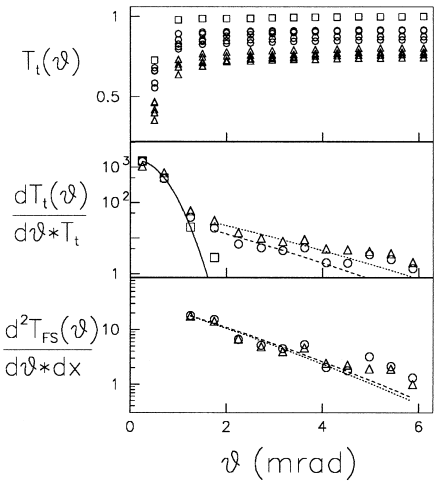

Fig. 5. Top panel: The intensity $T_0(\theta)$ (squares) of the 633 nm laser as a function of the opening angles of a diaphragm placed in front of the measuring diode, and the transmittance, at the same angles, through one $T_1(\theta)$ (circles) and two $T_2(\theta)$ (triangles) aerogel tiles hit at different points of the lateral surface. Central panel: Units in rad^{-1}. Laser beam profile (squares) with a Gaussian fit (solid line) and differential transmittances (circles and triangles) obtained by differentiating the average values of the data in the top panel and dividing by their respective linear transmittance (see text). The dashed and dotted lines are gaussian fits to triangles and circles at angles greater than 1 mrad. Bottom panel: Units in $\mathrm{rad}^{-1}\ \mathrm{cm}^{-1}$. The double differential transmittance for the forward scattering as a function of the scattering angle.

Differences in the transmittance values have been seen even for points hit only a few millimetres apart on the tile surface. By observing the image of the laser spot on a screen, one notices that the beam shapes emerging from one aerogel tile change from a leopard skin picture (a central spot surrounded by many others of smaller dimension and intensity and randomly distributed from 2 to 5 mrad away from the central spot), to a lobar shape (the beam is continuously distributed in one strip with a random direction up to 10 mrad). For this reason, only average values are given for the forward scattering. Fig. 5 shows the $T_t(\theta)$ transmittance measurements taken at different points on the front surface of an aerogel stack of total thickness t. Measurements for a stack of the same thickness are reported with the same symbols. The $T_t(\theta)$ values measured at large angles ($\theta = 6$ mrad) approach the 'linear' [11] transmittance $T_t(\theta_{\max})$, whose value is not influenced by the FS, but depends only on the Rayleigh scattering and absorption of the incident beam in aerogel.

The laser beam profile $\mathrm{d}T_0/\mathrm{d}\theta$ (squares in the central panel of Fig. 5), and the differential transmittances $\mathrm{d}T_t(\theta)/\mathrm{d}\theta$ (circles and triangles) are obtained by differentiating the quantities in the top part of Fig. 5. The latter differentials, normalized to $T_t(\theta_{\max})$ for removing the effect of Rayleigh scattering and absorption for detecting the FS effect, are shown in the central panel of Fig. 5 with circles and triangles, for the one and two tile measurements, respectively.

The beam profile is confined to angles smaller than 1.5 mrad, as shown by the solid curve in the central panel of Fig. 5, which represents a Gaussian fit to the squares. In contrast, the differential transmittances (circles and triangles) do extend at larger angles, indicating the modifications to the beam profile caused by the FS effect. A Gaussian fit to the circles and triangles at angles greater than 1 mrad is shown by the dashed and dotted lines, respectively.

The differential FS effect is derived by fitting the differential transmittances with a fraction (f_B) of the beam profile

$$\frac{\mathrm{d}T_{\mathrm{FS},t}(\theta)}{\mathrm{d}\theta} = \frac{\mathrm{d}T_t(\theta)}{\mathrm{d}\theta}\frac{1}{T_t} - f_B\frac{\mathrm{d}T_0}{\mathrm{d}\theta} \tag{10}$$

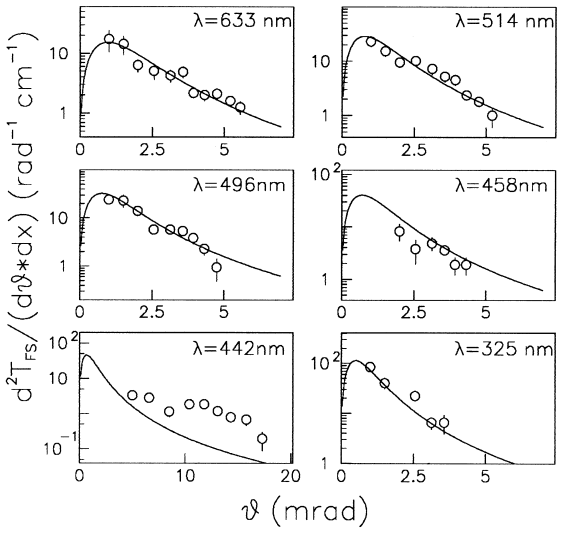

Fig. 6. The forward scattering double differential transmittance through aerogel as a function of the photon wavelength. The solid lines were obtained from Eq. (12), all calculated with $a_c = 60$ μm and a normalization factor $f = 0.4$ nm/(rad cm).

and the FS double (in angle and aerogel thickness) differential transmittances are obtained by dividing for the aerogel thickness t

$$\frac{\mathrm{d}^2T_{\mathrm{FS}}(\theta)}{\mathrm{d}\theta\,\mathrm{d}x} = \frac{\mathrm{d}T_{\mathrm{FS},t}(\theta)}{\mathrm{d}\theta}\frac{1}{t}. \tag{11}$$

These quantities are reported in the bottom panel of Fig. 5. The dashed and dotted lines in this panel are Gaussian fits to the $\mathrm{d}^2T_{\mathrm{FS}}(\theta)/\mathrm{d}\theta\,\mathrm{d}x$ values derived by measuring stacks of one and two aerogel tiles (circles and triangles, respectively). Their perfect overlap indicates that the probability of a photon undergoing two FS scatterings is very unlikely in the aerogel thicknesses explored. Final FS values were obtained by averaging the two measurements, and are reported in the top left panel of Fig. 6 with the estimated errors. Values at angles smaller than 1 mrad are not reported since they are affected by large errors due to the presence of the residual incident beam.

Fig. 6 also shows (empty circles) the same experimental $\mathrm{d}^2T_{\mathrm{FS}}/(\mathrm{d}\theta\,\mathrm{d}x)$ values measured, as in Fig. 5, for all the remaining λ's.

The double differential distribution of forward scattered radiation can be described [16] by the Rayleigh–Debye (Mie) scattering theory, which is a generalization of the Rayleigh scattering

$$\frac{d^2T_{FS}}{d\theta\,dx} = \frac{(1+\cos^2\theta)}{\lambda^4}(\sin\theta)\,wf. \tag{12}$$

The first of these factors is proportional to the Rayleigh scattering, the $\sin\theta$ term converts intensities in differential transmittances ($d\Omega \to d\theta$), the w term is the correlation volume, and f is a dimensional constant normalization factor. For a random two-phase medium model, well suited for aerogel, w is given [16] by

$$w = \frac{8\pi a_c^3}{(1+a_c^2\cdot h^2)^2} \tag{13}$$

where a_c is the average extension of the inhomogenities, and

$$h = \frac{4\pi}{\lambda}\sin\frac{\theta}{2}. \tag{14}$$

When a_c is much smaller than λ, w becomes a constant and thus independent of the scattering angle θ. In this case, Eq. (12) becomes the Rayleigh law. The scattered intensity is symmetrical with respect to $\theta = \pi/2$ and proportional to $1/\lambda^4$, as shown by the bottom panels of Fig. 7. For a_c much greater than λ, the scattering becomes forward peaked (see the top panels of Fig. 7) and nearly constant with λ.

The experimental data contained in Fig. 6 are well fitted by Eq. (12) evaluated for $a_c = 60 \pm 10$ μm and $f = 0.4 \pm 0.1$ nm/(rad cm). The fits obtained are displayed with solid lines in Fig. 6. The value of the inhomogenities (a_c) obtained suggests a nearly constant FS value with λ. To show the difference between the curves in Fig. 6, they are reported in the top panel of Fig. 8 at selected wavelengths. Strong differences occur only below 3 mrad. In fact, the integrals over θ of these curves decrease by a factor of ten when the 0–6 mrad integration interval is considered, as shown by the solid curve in the second panel of Fig. 8. The decrease is reduced to a factor of 2 and 1.5 for the intervals 1–6 and 2–6 mrad, respectively (see the dashed and dotted lines).

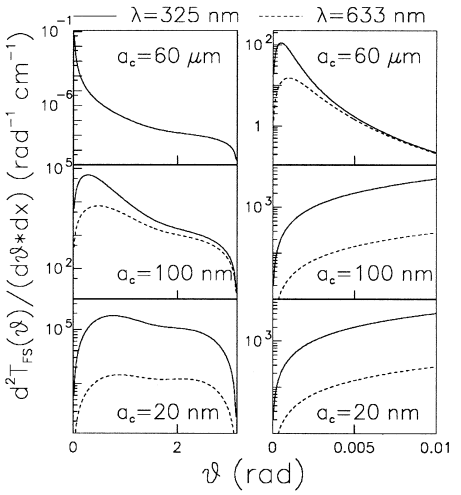

Fig. 7. The *FS* double differential transmittance through aerogel, calculated by Eq. (12) for the three indicated values of inhomogenities (a_c), and plotted in the whole θ-range (left-side) and at forward angles (right-side). The solid and dashed lines refer to wavelengths of 325 and 633 nm, respectively.

Since some of the measurements shown in Fig. 6 could not be performed at small angles, due to an increased laser divergence and spot dimension, the $T_{FS,1}$ values, i.e., the integral over θ (1–6 mrad) and 1 cm of aerogel of the experimental $d^2T_{FS}/(d\theta\,dx)$, are obtained from only the $\lambda = 633$, 514, 496, and 325 nm measurements. These values are shown with full squares in the second panel of Fig. 8 and show a weak λ-dependence.

A good agreement in the second panel of Fig. 8 is shown among the experimental T_{FS}'s and the calculated dashed curve. But the best estimation of the FS effect at the different λ's comes from the solid curve in the second panel of Fig. 8, which considers also the very small angles that are experimentally unreacheable. The mean value of this curve was calculated by weighting it with the photoelectron distributions shown in Fig. 3. An average forward scattering value of $T_{FS,1} = 15 \pm 3\%$ is obtained for HERMES, and $17 \pm 3\%$ for LHCb.

From the curves in the top panel of Fig. 8, the average forward scattering angle (θ_{FS}) at the different wavelengths was calculated and is reported in the third panel of Fig. 8. This quantity, averaged over the photoelectron distributions in Fig. 3, gives

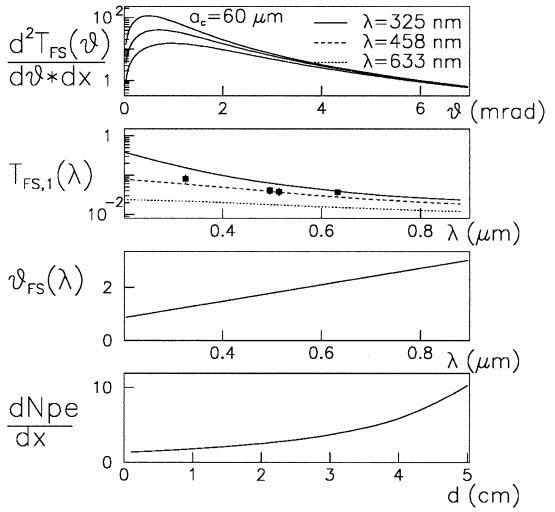

Fig. 8. Top panel: Units in $\mathrm{rad}^{-1}\ \mathrm{cm}^{-1}$. The forward scattering double differential transmittance through aerogel, calculated from Eq. (12) with $a_c = 60$ μm and a normalization factor $f = 0.4$ nm/(rad cm), at the indicated wavelengths. Second panel: The integrals of the curves in the top panel evaluated over 1 cm of aerogel and over different angular intervals of integration: 0–6, 1–6, and 2–6 mrad, for the solid, dashed, and dotted lines, respectively. The integrals of the experimental values in Fig. 6 are reported by full squares. Third panel: Units in mrad. The average forward scattering angle evaluated from the curves in the top panel. Bottom panel: Units in cm^{-1}. The differential number of photoelectrons produced at different positions in a stack of five aerogel tiles with a total thickness of 5 cm.

a mean forward scattering angle value of $\theta_{FS} = 1.55$ mrad for HERMES, and 1.48 mrad for LHCb.

To evaluate the fraction of Cherenkov photons produced in a stack of aerogel tiles (total thickness t) and scattered at forward angles whilst travelling in the same stack, the spatial distribution of the Cherenkov photoelectrons was evaluated by considering the double differential Cherenkov production yield ($\mathrm{d}^2N/\mathrm{d}\lambda\,\mathrm{d}x$), the probability that Cherenkov photons produced at the point x escape aerogel through the exit face at a distance $t - x$, and the quantum efficiency of the photodetector, as

$$\frac{\mathrm{d}N_{\mathrm{pe}}}{\mathrm{d}x} = \int \frac{\mathrm{d}^2N}{\mathrm{d}\lambda\,\mathrm{d}x} T_{t-x}(\lambda)\mathrm{q.e.}(\lambda)\,\mathrm{d}\lambda. \tag{15}$$

This spatial distribution, evaluated for $\beta = 1$ particles, is reported in the third panel of Fig. 8 for stacks (t) of 5 cm. The averaged thickness of aerogel crossed by Cherenkov photons, calculated from this distribution, is $t_{\mathrm{av}} = 1.62$ cm, denoting that ($\bar{T}_{\mathrm{FS},t} = \bar{T}_{\mathrm{FS},1}\, t_{\mathrm{av}}$) $23 \pm 4\%$ of the Cherenkov photons produced in the aerogel stacks of the HERMES RICH are scattered at the average angle $\theta_{\mathrm{FS}}(\bar{\lambda}) = 1.55$ mrad from their primary θ_{C} direction. The remaining 76% Cherenkov photons do no deflect from the θ_{C} direction. This depicted angular distribution of photoelectrons in the Cherenkov ring has a standard deviation ($\Delta\theta_{\mathrm{FS}}$) of 0.77 mrad. For LHCb an increased $T_{\mathrm{FS},\bar{t}}(\bar{\lambda})$ value ($27 \pm 4\%$) is obtained, but $\Delta\theta_{\mathrm{FS}}$ (0.79 mrad) is nearly the same.

The contribution to the ring resolution due to the forward scattering is

$$\left(\frac{\delta\theta}{\theta}\right)_{\mathrm{FS}} = \left(\frac{\Delta\theta_{\mathrm{FS}}}{\theta_{\mathrm{C}}}\right)\frac{1}{\sqrt{N_{\mathrm{pe}}}}. \tag{16}$$

Therefore, the dispersion resulting from the forward scattering effect is 0.10% for HERMES and 0.08% for LHCb.

4. Aerogel forward scattering length

The forward scattering transmittance $T_{\mathrm{FS},t}$ was measured by means of a spectrophotometer equipped with an integrating sphere. Measurements were taken in the 200–900 nm wavelength range by means of a CARY-5 (from Varian) spectrophotometer, and an integrating sphere (from Labsphere). The sphere, covered internally with Spectralon, a material with high and near-Lambertian reflectivity, is able to convey all the light reaching its internal surface to a photomultiplier (PM port) as shown in Fig. 9. The linear transmittance (T_t) is measured by using a beam of large transversal dimensions, housing the aerogel sample outside the sphere very near to its input port, and by inserting the output plug to the sphere, as shown in the top panel of Fig. 9. The 'diffuse' transmittance at forward angles ($T_{\mathrm{diff},t}$) is measured with a beam of small transversal dimensions and divergence, obtained by several collimators on the beam before the aerogel, and with the output plug of the sphere removed (see the bottom panel of Fig. 9).

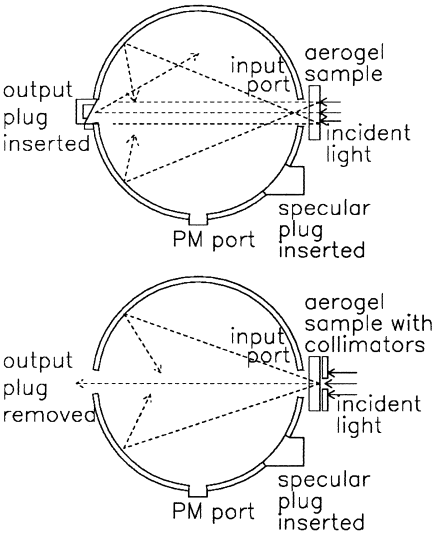

Fig. 9. The integrating sphere equipped for 'linear' transmittance (top panel) and 'diffuse' transmittance (bottom panel) measurements.

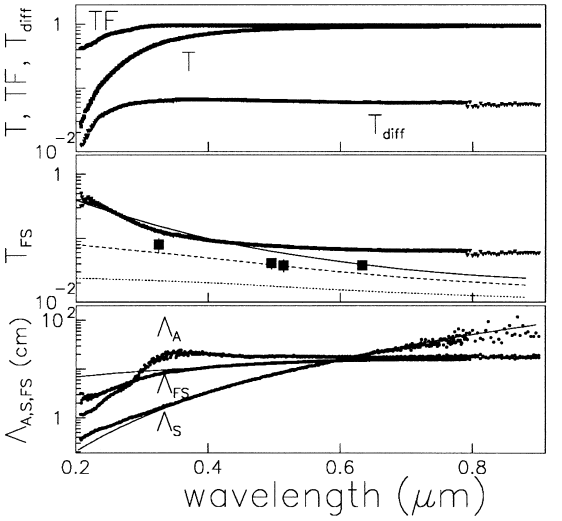

Fig. 10. Top panel: The linear (T) and diffuse (T_{diff}) transmittances, together with the transflectance (TF, taken from Ref. [11]) for light trough 1 cm of aerogel. Central panel: The forward scattering transmittance deduced from the experiments in the top panel (marked curve) and taken from the second panel of Fig. 8 (squares, and full, dashed, and dotted lines). Bottom panel: The aerogel absorption, Rayleigh scattering, and forward scattering lengths, evaluated from the curves in the top panels through Eq. (18). The Rayleigh and forward scattering lengths are fitted with phenomenologic curves, requiring a λ^4- and a $\lambda^{0.65}$-dependence, respectively.

The linear, the diffuse, and the forward scattering transmittances are linked by the relation

$$T_{\mathrm{diff},t} = T_{\mathrm{FS},t}\, T_t. \tag{17}$$

$T_{\mathrm{FS},t}$ is the fraction of incident light that experiences in forward scattering, $T_{\mathrm{diff},t}$ is what one measures of the forward scattering considering the attenuation (T_t) of the incident beam from the aerogel front face up to the point where a forward scattering event occurs, and of the forward scattered beam on its way from the production point to the aerogel exit face.

The measured linear (T_t) and diffuse ($T_{\mathrm{diff},t}$) transmittances for an aerogel tile of thickness 1 cm, are reported in the top panel of Fig. 10. The reported $T_{\mathrm{diff},t}$ is an average of several measurements at different points on the tile. The 'transflectance' (TF_t), which is the measurement of the light percentage surviving the absorption ($\mathscr{A}_t$) in a sample, is also reported in Fig. 10. Absorption and transflectance are linked by the simple relation: $\mathscr{A}_t = 1 - \mathrm{TF}_t$. The TF_t measurement is taken from Ref. [11]. All the data in the top and central panels of Fig. 10 refer to 1 cm of aerogel. The subscript 1 has been omitted.

In the central panel of Fig. 10, the forward scattering transmittance, deduced from Eq. (17) and from the data in the top panel of the figure, is shown with a marked curve. The content of the second panel of Fig. 8, namely the experimental $T_{\mathrm{FS},t}$'s (full squares), and the calculated $T_{\mathrm{FS},t}$'s (solid, dashed, and dotted lines) is also reported in the central panel of Fig. 10. The experimental values from the integrating sphere (marked curve) are higher than those from the previous section (full squares). This disagreement could be due to the larger θ-opening allowed by the input port of the sphere compared to that of the diaphragm in Fig. 4. However the experimental values from the integrating sphere agree up to 500 nm with the calculated values (solid line).

The TF, T, and T_{FS} are linked to the three $\Lambda_{\mathrm{A,S,FS}}$ (absorption, Rayleigh scattering, and forward scattering, respectively) lengths by the simple

relations

$$\mathrm{TF} = \mathrm{e}^{-1/\Lambda_A}, \quad T = \mathrm{e}^{-t(1/\Lambda_A + 1/\Lambda_S)} = \mathrm{e}^{-1/\Lambda},$$
$$T_{FS} = 1 - \mathrm{e}^{t/\Lambda_{FS}}. \tag{18}$$

In the bottom panel of Fig. 10 the three lengths obtained for aerogel are reported. The Λ_S curve is fitted by a λ^4-dependence, whilst the Λ_{FS} one requires a weaker $\lambda^{0.65}$-dependence. The Λ_A curve is constant in the interval 350–900 nm.

5. Cherenkov angle resolution of the HERMES and LHCb RICH detectors

The HERMES RICH detector employs aerogel tiles from Matsushita with a total thickness of 5 cm, spherical mirrors with a radius of 220 cm, and 3/4″ Philips XP1911 photomultipliers mounted with aluminized Mylar funnels of 1″ diameter (D).

The LHCb RICH detector employs aerogel of the same thickness and type as the HERMES one, spherical mirrors with a radius of 200 cm, and hybrid photodiodes with a pixelization of 2.5×2.5 mm^2.

The Cherenkov angle resolution due to the pixelization of the focal plane detector, for photodetectors of circular shape D and Cherenkov rings of radius R, is

$$\left(\frac{\delta\theta}{\theta}\right)_{\mathrm{pixel}} = \left(\frac{D}{4R}\right)\frac{1}{\sqrt{N_{\mathrm{pe}}}}. \tag{19}$$

In HERMES, the pixel diameter is $D = 2.54$ cm, and $R = 27.7$ cm. A value $(\delta\theta/\theta)_{\mathrm{pixel}} = 0.075\%$ is obtained, corresponding to 5.7 mrad. For the squared photodiodes of LHCb, the pixel resolution is 0.18 mrad.

The fluctuation in the refractive index of the different Matsushita aerogel tiles was measured at 633 nm [17] and found equal to $\delta n/(n-1) = 1.3\%$. This value can be reduced to 0.54% by sorting tiles with similar refractive indices in the same stack (each with $m = 5$ tiles), as in the HERMES RICH. This contribution to the resolution, which is position-independent, is given [12,13] by

$$\left(\frac{\delta\theta}{\theta}\right)_{\mathrm{pos.indep.}} = \frac{1}{2}\frac{\delta n}{n-1}\frac{1}{\sqrt{N_{\mathrm{pe}}}}. \tag{20}$$

The density fluctuation of the Matsushita aerogel was measured in Refs. [12,13]. Its contribution to the resolution, which is position-dependent, is expressed by:

$$\left(\frac{\delta\theta}{\theta}\right)_{\mathrm{density}} = \frac{1}{2}\frac{\delta\rho}{\rho}\frac{1}{\sqrt{N_{\mathrm{pe}}}}. \tag{21}$$

A value of 0.39%/pe was found.

All the Matsushita aerogel tiles have one flat and one curved surface caused by capillary effects during manufacturing. These effects are more important at the tile borders. Photons leaving the tile through the curved surface are dispersed by $\Delta\theta_S$, which is the average angle between the normals to the curved surface and the tile axis. Measuring two tiles, excluding the borders (5 mm), resulted in $\Delta\theta_S = 0.5$ mrad. To limit this dispersion, the tiles must be stacked with the curved surface facing the incoming beam. In HERMES the tiles were stacked randomly, and from the $\mathrm{d}N_{\mathrm{pe}}/\mathrm{d}x$ distribution in Fig. 8, it follows that 24, 36, 24, 12, and 4% of Cherenkov photons leave the stacks passing through 0, 1, 2, 3, and 4 curved surfaces, respectively. The standard deviation of this distribution is $1.2\Delta\theta_S$. Then the surface dispersion is

$$\left(\frac{\delta\theta}{\theta}\right)_{\mathrm{surface}} = \frac{1.2\Delta\theta_S}{\theta_C}\frac{1}{\sqrt{N_{\mathrm{pe}}}}. \tag{22}$$

The full length of the radiator and the uncertainty in the photon emission point contribute to the ring resolution. These (point) uncertainties have been estimated in Refs. [5–8] by a Monte Carlo calculation. A value of 0.32%/pe was found.

All the contributions considered in this paper are reported in Table 1. Their total sum is 1.3%/pe for LHCb and 2.5%/pe for HERMES. The total number of photoelectrons (N_{pe}) reported in Table 1 is estimated for LHCb, and measured for HERMES. From these the total calculated resolutions have been deduced. For HERMES the measured resolution is also reported in Table 1.

For LHCb the calculated total resolution (0.34%) is dominated by the chromatic aberration. For HERMES the calculated total resolution (0.84%) is dominated by the pixel contribution. A slightly higher value (1.2%) was measured.

Table 1
The different contributions, in percent, to the aerogel Cherenkov angle resolution for the HERMES and LHCb RICH detectors, and their total values

Resolution	HERMES	LHCb
Pixel/pe	2.30	0.29
Pos.indep./pe	0.27	0.27
Density/pe	0.39	0.39
Surface/pe	0.24	0.24
Point/pe	0.32	0.32
Chromatic/pe	0.74	1.05
Forw.scatt./pe	0.31	0.32
Total/pe	2.52	1.30
N_{pe}	9	15
Total (calc.)	0.84	0.34
Total (exp.)	1.2	–

An effect similar to forward scattering also occurs for photons reflected by the mirrors (reflection at small angles from the Snell angle or diffused mirror reflection). In Ref. [10] a high contribution from this effect was hypothesized to fit the experimental ring angle resolution obtained by using aerogel and mirrors different from those referred to this paper. This contribution, and others from the mirrors, are more relevant for LHCb than for HERMES.

6. Conclusions

This paper deals with the chromatic aberration and forward scattering contributions to the Cherenkov angle resolution of RICH detectors with radiators of silica aerogel.

For this purpose, the refractive index and the double (in angle and aerogel thickness) differential scattering of light at forward angles (not Rayleigh) were measured in the range from 350 to 650 nm for the Matsushita aerogel used in the HERMES and LHCb RICH detectors.

In the λ-interval explored, the refractive index of aerogel decreased by 0.15%. Moreover, a difference of 0.0008 was found between the refractive index of the aerogel measured at the usual wavelength of 633 nm and its value at 400 nm, which is the average wavelength converted in photoelectrons in the HERMES and LHCb RICH detectors.

The hypothesis of Vorobiov et al. [14], suggesting a constant ratio between the refractive indices of aerogel and its constituents, air and quartz, has been verified to be a good approximation in the λ-interval explored here.

Light in aerogel is deviated by the forward scattering effect at average angles ranging from 1.2 mrad at 400 nm, to 2.2 mrad at 700 nm. The fraction of deflected photons by 1 cm of aerogel varies from 20% to 8% at these two wavelengths, respectively. The wavelength dependence of the forward scattering in aerogel was also measured by a spectrophotometer equipped with an integrating sphere. From this measurement, the forward scattering length in aerogel was deduced and found to have a weak λ-dependence ($\lambda^{0.65}$).

The chromatic aberration and forward scattering effect contribute to the aerogel Cherenkov angle resolution, both for the HERMES and for the LHCb RICH detectors, with values around 1% and 0.3% per photoelectron, respectively.

Total resolutions of 0.84% and 0.34% were estimated for the two aforementioned RICH detectors, respectively.

Acknowledgements

The authors are grateful to the HERMES RICH Collaboration for their interest in this work and also to Dirk Ryckbosch and Harold Jackson for fruitful discussions about the manuscript.

References

[1] I. Adachi et al., Nucl. Instr. and Meth. A 355 (1995) 390.
[2] H. Yokogawa, M. Yokoyama, J. Non-Cryst. Solids 186 (1995) 23.
[3] J. Seguinot, T. Ypsilantis, Nucl. Instr. and Meth. A 368 (1995) 229.
[4] LHCb, Technical Proposal, CERN/LHCC 98-4, 1998.
[5] R. De Leo et al., Proposal to add a Ring Imaging Cherenkov detector to HERMES, Report INFN-ISS 96/9.
[6] E. Cisbani et al., Proposal for a dual radiator RICH for HERMES, DESY HERMES Note 97-003.
[7] E. Cisbani et al., Proceedings of the 36th Workshop of the INFN Eloisatron Project, Erice 'Italy' 1–7 Nov. 1997, World Scientific, Singapore.

[8] D. Ryckbosch, Nucl. Instr. and Meth. A 433 (1999) 98.
[9] K. Ackerstaff et al., HERMES Collaboration, Nucl. Instr. and Meth. A 417 (1998) 230.
[10] R. De Leo et al., Nucl. Instr. and Meth. A 401 (1997) 187.
[11] E. Aschenauer et al., Optical characterization of $n = 1.03$ silica aerogel used as radiator in the RICH of HERMES, Nucl. Instr. and Meth. A 440 (2000) 338.
[12] P. Carter, Nucl. Instr. and Meth. A 433 (1999) 392.
[13] P. Carter, The HERMES experiment, Ph.D. Thesis, California Institute of Technology, Pasadena, California, HERMES Internal Report No. 99-013, 1999.
[14] V.I. Vorobiov et al., Proceedings of the Workshop on Physics and Detectors for DAPHNE, Report INFN-Frascati, 1991.
[15] M. Born, E. Wolf, Principles of Optics: Electromagnetic Theory of Propagation, Interference and Diffraction of Light, Cambridge University Press, Cambridge, ISBN: 0521639212.
[16] P. Wang, W. Korner, A. Emmerling, A. Beck, J. Kuhn, J. Fricke, J. Non-Cryst. Solids 145 (1992) 141.
[17] J. Kanesaka, L.F. Zhang,Y. Sakemi, K. Suetsugu, F. Sato, T.-A. Shibata, Measurements of the Properties of Silica Aerogel Tiles for HERMES RICH, HERMES Internal Report No. 98-061, 1998.